Utilizing a Multi-Proxy to Model Comparison to Constrain the Season and Regionally Heterogeneous Impacts of the Mt. Samalas 1257 Eruption

Laura Wainman[1,2], Lauren R Marshall[3,4], Anja Schmidt[3,5,6]

5   [1]Department of Earth Sciences, University of Cambridge, Cambridge, CB2 3EQ, UK
[2]School of Earth and Environment, University of Leeds, Leeds, LS2 9JT, UK
[3]Yusuf Hamied Department of Chemistry, Cambridge, CB2 1EW, UK
[4]Department of Earth Sciences, Durham University, Durham, DH1 3LE, UK
[5]Institute of Atmospheric Physics (IPA), German Aerospace Centre (DLR), Oberpfaffenhofen, 82234, Germany
10   [6]Meterological Institute, Ludwig Maximilian University of Munich, Munich, 80333, Germany

Correspondence to: Laura Wainman (eelrw@leeds.ac.uk)

Abstract. The Mt. Samalas eruption, thought to have occurred between 1257 and 1258, ranks as one of the most explosive sulfur-rich eruptions of the Common Era. However, the precise year and season of the eruption remains unconstrained with evidence indicating both summer 1257 and early 1258 as potential eruption dates. Widespread surface cooling and

15 hydroclimate perturbations following the eruption have been invoked as contributing to a host of 13th Century social and economic crises, although regional scale variability in the post-eruption climate response remains uncertain. In this study we run ensemble simulations using the UK Earth System Model (UKSEM1) with a range of eruption scenarios and initial conditions in order to compare our simulations with the most complete globally resolved multi-proxy database for the Mt. Samalas eruption to date, incorporating tree-ring, ice core, lake sediment, and historical records. This allows more-precise

20 constraints to be placed on the year and season of the Mt. Samalas eruption as well as an investigation into the regionally heterogeneous post-eruption climate response. Using a multi-proxy to model comparison, we are able to robustly distinguish between July 1257 and January 1258 eruption scenarios where the July 1257 ensemble simulation achieves considerably better agreement with spatially averaged and regionally resolved proxy surface temperature reconstructions. These reconstructions suggest the onset of significant cooling across Asia and Europe in 1258, and thus support the plausibility of

25 previously inferred historical connections. Model-simulated temperature anomalies also point to severe surface cooling across the Southern Hemisphere with as of yet unexplored historical implications for impacted civilizations. A re-evaluation of the use of ice core sulfate deposition records to constrain eruption season and volcanic stratospheric sulfur injection (VSSI) estimates also highlights current limitations in this approach, with our model simulations revealing distinct differences in the timing and magnitude of the ice sheet deposition between the two seasons. Overall, the multi-proxy to

30 model comparison employed in this study has strong potential in constraining similar uncertainties in eruption source parameters for other historical eruptions where sufficient coincident proxy records are available.

1 Introduction

The Mt. Samalas eruption, which occurred on the Indonesian Island of Lombok between 1257 and 1258, is identified in ice
35   cores as one of the largest volcanic sulfate deposition events of the last 2500 years (Palais et al., 1992, Zielinski et al., 1994).
Petrological analysis suggests a release of ~120Tg of sulfur dioxide (SO2) into the stratosphere, with a maximum estimated
plume height of 43 km and volcanic explosivity index (VEI) of 7, meaning the eruption ranks as one of the most-explosive
sulfur-rich eruptions of the Common Era (Lavigne et al., 2013, Vidal et al., 2015, Toohey and Sigl, 2017). Tree-ring
reconstructions suggest a peak Northern Hemisphere (NH) average summer cooling of -0.8°C to -1.2°C between Summer
40   1258 and 1259 (Wade et al., 2020, Guillet et al., 2017, Wilson et al., 2016, Büntgen et al,. 2022). The surface air temperature
(SAT) anomalies and potential hydroclimate perturbations induced by the eruption have been invoked by historians as
contributing factors to a host of 13th Century social and economic crises (Campbell, 2017, Malawani et al., 2022, Guillet et
al., 2017, Bierstedt, 2019, Stothers 2000, Fell et al., 2020, Kern et al., 2021).

45   Summer 1257 and January 1258 are the two most commonly cited dates for the Mt. Samalas eruption, however, as of yet, no
single suite of evidence has been able to robustly distinguish the precise year and season of the eruption. The full span of
dates proposed ranges from 1256 to 1258, however the earliest date of Spring 1256 was based on historical evidence for a
dust veil over Asia and the Middle East in late 1256 and early 1257 (Bauch, 2019). This is more likely attributed to a smaller
eruption such as the 1256 Medina eruption which had only localized impacts (Saliba, 2017). A mid-1257 eruption date was
50   first proposed by Oppenheimer (2003) based on the spatial distribution of negative temperature anomalies across both
hemispheres for 1257-59, with radiocarbon dating of the pyroclastic flow deposits associated with the eruption also yielding
an earliest date of 1257. Based on the westerly displacement of ash isopachs, Lavigne et al., (2013) proposed that easterly
winds prevailed at the time of the eruption, indicative of the eruption occurring during the May-Oct dry season. Büntgen et
al., (2022) also show that the earliest onset of potential tree-ring width (TRW) growth anomalies in the Western US occur in
55   the late 1257-growth season, adding their support for an eruption date prior to August 1257. Modelling studies for the Mt.
Samalas eruption have achieved best agreement with tree-ring reconstructions for a May-July eruption window (Stoffel et
al., 2015). Nonetheless, peak sulfate deposition in ice cores is recorded for 1259 and the first historical reports of a dust veil
over Europe appear in Summer 1258, which has been suggested to be most compatible with an early 1258 eruption (Stothers
2000). Therefore, there is still a need to constrain the year and season of the eruption with greater certainty, with
60   implications for evaluating the robustness of inferred connections to synchronous historical events, as well as in the role of
the eruption sulfate deposition spike as a key temporal calibration marker in ice core records.

The regionally heterogeneous climate response to the Mt. Samalas eruption also remains largely unconstrained at a global
level. Guillet et al., (2017) utilized a wealth of historical records and tree-ring chronologies to assess the impact of the
65   eruption across the NH, with particular focus on the climate response to the eruption revealed by historical sources in

Western Europe. Medieval chronicles point to abnormal weather conditions in Summer 1258, with economic records highlighting delayed and poor harvests which likely aggravated ongoing grain shortages. Stothers (2000) suggested that frequently cold and rainy weather lead to widespread crop damage and famine, also noting the outbreak of plague across Europe and the Middle East in 1258-59. It has also been suggested that the epidemiological progression of Y. pestis, the

70 bacterium responsible for the Black Death, can be traced to the climatic perturbations associated with the Mt. Samalas eruption (Fell et al., 2020). The climatic aftereffects of the eruption may have also included a shift in the Asian Monsoon and therefore be linked to the series of epidemics, droughts, and famines, associated with the decline of the Mongol Empire (Kern et al., 2021). Nonetheless, without a comprehensive globally resolved understanding of the climate response to the eruption the robustness of these inferred connections between post-eruption climate response and historical events remains

75 difficult to constrain.

The magnitude and spatial distribution of the post-eruption climate response following large volcanic eruptions in known to show a strong seasonal dependency (Stevenson et al., 2017, Toohey et al., 2011). Asymmetric cooling between hemispheres occurs due to seasonal variation in Brewer-Dobson circulation which modulates hemispheric aerosol distribution (e.g

80 Toohey et al., 2011). Asymmetric aerosol distribution combined with enhanced land-albedo feedbacks during NH winter can therefore increase the magnitude of temperature anomalies between hemispheres (Stevenson et al., 2017). Hemispheric temperature contrasts can subsequently drive latitudinal shifts in the Inter-Tropical Convergence Zone (ITCZ), an equatorial band of enhanced rainfall and lower pressure, away from the hemisphere of greatest cooling resulting in hydroclimate perturbations (Broccoli et al., 2006). Therefore, depending on if the Mt. Samalas eruption occurred in Summer 1257 or in

85 early 1258, differences in the magnitude and spatial distribution of resulting SAT and precipitation anomalies are expected.

In this study we utilize a multi-proxy to model comparison to place more precise constraints on the year and season of the Mt. Samalas eruption, tested across the whole window of proposed eruption dates. We utilize both model and proxy constraints to assess regionally heterogeneous impacts of the Mt. Samalas eruption, with reference to proposed historical

90 consequences. UK Earth System Model (UKESM1) simulations were run across January and July eruption scenarios and a globally resolved database of proxy records was collated consisting of tree-ring chronologies, historical sources, lake sediments, and ice core records (Supplementary Sheet 1). This constitutes the most complete multi-proxy database for the Mt. Samalas eruption to date. Our study demonstrates the ability of a multi-proxy to model comparison to more precisely constrain the date of the Mt. Samalas eruption, where previous studies have tended to utilize only a single-proxy approach

95 (Stothers, 2000, Bauch, 2019, Büntgen et al., 2022, Stoffel et al., 2015). The multi-proxy to model comparison employed in this study is shown to have significant potential in constraining similar uncertainties in eruption source parameters for other historical eruptions where sufficient coincident proxy records are available.

2 Methods

2.1 Model Simulations Using the UK Earth System Model (UKESM)

The state-of-the-art interactive aerosol-climate model UKESM1 (Sellar et al., 2019) was used, consisting of the physical global climate model HadGEM3-GC3.1 with additional configurations for terrestrial and marine biogeochemistry, land and ocean physics, ocean-sea ice, and dynamic terrestrial vegetation. The model also includes the UK Chemistry and Aerosol (UKCA) interactive stratospheric-tropospheric chemistry and aerosol schemes (Archibald et al., 2020, Mulcahy et al., 2020). The full life cycle of stratospheric sulfur and sulfate aerosol particles is included, from injection of SO_2, oxidation, particle formation and subsequent growth, to sedimentation and removal.

The model has a horizontal atmospheric resolution of 1.875° by 1.25° and a 1° by 1° resolution in the ocean, giving a vertical resolution of 85 levels in the atmosphere and 75 levels in the ocean. This results in well-resolved ocean and atmosphere dynamics and an internally generated Quasi-Biennial Oscillation (QBO). Coupled ocean-atmosphere simulations were run with greenhouse gases set to a representative pre-industrial (AD 1850) background state. The difference between a preindustrial and bespoke 13th century background state is small compared to model internal variability and thus does not represent a significant limitation of the approach.

Eighteen UKESM eruption-perturbed ensemble simulations were run, with nine simulating a January eruption and nine a July eruption, where January and July are winter/summer representatives. Given the preindustrial background the January/July ensemble groupings are not constrained to a specific year and therefore the two ensemble groupings have been used to assess the full range of dates proposed for the Mt. Samalas eruption between the years 1256 and 1258. The ensembles sample a range of initial conditions, with the starting phase of both QBO and the El Niño Southern Oscillation (ENSO) varying between ensembles. For full details of ensemble initial condition classification see Supplementary Document Table S1. Across the eighteen ensembles only the eruption season and initial conditions were varied, with all other eruption source parameters held constant and as listed in Table 1.

119 Tg of SO_2 was taken from the updated database of VSSI estimates (eVolv2k; Toohey and Sigl, 2017), which is within error of the 126 +/- 9.6 Tg estimated by Vidal et al. (2016). In our simulations, the injection height is set at 18-20 km to be consistent with the 1991 Mt. Pinatubo eruption and to allow for lofting of aerosol to higher altitudes in the stratosphere. This height is lower than the estimated 38-40 km column heights (Lavigne et al., 2013, Vidal et al., 2015) however, those column heights refer to the maximum altitude of tephra and ash rather than the height of sulfur injection in the stratosphere or the maximum altitude of the SO_2 plume. A 24-hr eruption duration agrees well with Lavigne et al., (2013) who estimated the eruption duration to be 23.8 +/- 10.3 hrs.

An equivalent control ensemble, with identical starting conditions but no eruption perturbation, was run for each of the individual eruption-perturbed ensemble simulations. Anomalies were calculated with respect to a climatological background constructed from the control ensemble mean.

135

Table 1: Eruption Source Parameter values used in the ensemble simulations.

Eruption Source Parameter	Ensemble Value
Volcanic stratospheric sulfur injection (VSSI)	119 Tg of SO_2
Injection Height	18-20 km
Duration	24hrs
Latitude	8°S

2.2 Multi-Proxy Database of Surface Temperature Impacts

The proxy database (See Supplementary Sheets 1 and 2 for full details) was constructed by compiling records indicative of changes to climate (tree-ring chronologies, ice core records, lake sediments and historical sources) that span the range of

140   dates proposed for the eruption with a minimum of annual resolution. Whilst the aim was to create a global database of proxy records, this was significantly impeded by the limited global distribution of all types of proxy records, which show a strong bias to the NH, European, and North American localities. No suitable data was found for this study from Africa or South America.

2.2.1 Tree-Ring Chronologies

145   We include 24 region-specific tree-ring studies, distributed predominantly across the NH, although two studies from Australia and New Zealand are included. The parameter used for temperature reconstruction varies between studies, as does the tree species analyzed and season of reconstruction depending on study location (see Supplementary Sheet 1 for details). SAT anomalies for 1258 and 1259 were taken either directly from the referenced study or calculated from reconstructed SAT anomalies using a background climatology which was constructed from the 10-year average prior to the eruption. Where

150   studies reported that frost rings were present, they have also been included in the database.

In addition to the 24 region-specific studies, four NH spatially averaged reconstructions have also been incorporated (Wilson et al., 2016, Schneider et al., 2015, Büntgen et al,. 2021, Guillet et al., 2017), along with the N-TREND reconstruction which is spatially resolved for the NH (Anchukaitis et al., 2017). For consistency in this study all tree-ring-reconstructed SAT

155   anomalies are calculated from the 10-year average prior to 1257.

2.2.2 Ice Core Records

We include two ice core records of SAT derived from annually resolved $\delta^{18}O$ isotope series. The first, from Greenland, record is from analysis by Guillet et al., (2017) who utilized three Greenland ice cores at GRIP, CRETE, and DYE3 (Vinther et al., 2010) to calculate an average SAT anomaly for 1258. The second, from Svalbard, is also derived from annually resolved isotope records and calibrated against instrumental measurements (Divine et al., 2017). Additional ice core records were investigated to expand this analysis such as the Illimani Ice Core in Bolivia and the Belukha Ice Core in Altai, Siberia; however, both records lacked the annual resolution required to constrain abrupt temperature changes associated with volcanic eruptions.

2.2.3 Lake Sediments

Two lake sediment records are also included from the Gulf of Alaska (Loso, 2008) and Baffin Island (Moore et al., 2001). Both studies measure sediment varve thickness, which varies annually, to calculate yearly summer SAT anomalies. Variations in varve thickness result from strong seasonal fluctuations in runoff and sediment fluxes during the summer melt season. Both studies demonstrate significant correlation between varve thickness and instrumentally measured June-July-August (JJA) Summer temperatures.

2.2.4 Historical Sources

Historical sources consist predominantly of medieval chronicles which refer to abnormal and/or extreme weather events in the years 1258-59. Analysis of medieval chronicles and economic records for the years 1258-59 by Guillet et al., (2017) form the basis of historical constraints in Europe. Additional chronicles include references from the Russian Annals in the Altai Mountains (Borisenkov and Pasetsky, 1988, Guillet et al., 2017), the Chronicle of Novgorod from Central Russia (Stothers, 2000), the Þorgils Saga Skarða in Iceland (Bierstedt, 2019), and Azuma Kagami from Japan (Farris, 2006). References to abnormally dark lunar eclipses are also included from the Chronicle of the Abbey of St. Edmunds (Stothers, 2000) and the Annales Ianuenses (Guillet et al., 2017). Additional historical sources across Europe, as well as some from the Middle East, report plague, famine, and economic crises for 1258-60 (Stothers, 2000). These sources have not been incorporated into the database as they refer to social and economic disturbances rather than making direct references to abnormal climatological phenomena.

2.3 Simulated SAT Anomalies

2.3.1 Northern Hemisphere Average

Spatially averaged NH summer land SAT anomalies were calculated for the mean of the nine July and January Ensembles respectively. Constraints were applied to model-simulated surface temperature outputs to make them most comparable to tree-ring reconstructions (Latitudes of 40°N-75°N, land only, June-July-August (JJA) was taken as representative of the

growth season.) Using four NH spatially averaged tree-ring chronologies (Wilson et al., 2016, Schneider et al., 2015, Büntgen et al., 2021, Guillet et al., 2017 – see Supplementary Document, Figure S1 for individual chronology comparison) a mean NH summer SAT anomaly timeseries was also calculated to which the model-simulated anomalies are compared.

2.3.2 Spatially Resolved Comparison

190 Spatially resolved model-simulated summer (JJA) SAT anomalies were calculated globally and for the NH between 1258-1259. This time window was chosen because the July 1257 and January 1258 ensemble simulations show the greatest divergence in SAT anomalies for Summers 1258-59. Model-simulated NH SAT anomalies were re-gridded and masked to facilitate more direct comparison with the N-TREND dataset (Anchukaitis et al., 2017). An analysis of variance (ANOVA) test was performed by eruption season to determine at which grid points the variance in means between the 1258 and 1259

195 perturbed ensembles exceeded 95% significance relative to the control ensemble simulations, where the null hypothesis was that there was no difference between the mean grid point anomalies for the perturbed 1258 and 1259 ensembles compared to the control ensemble.

3. Results

3.1 Multi-Proxy to Model Comparison

200 ### 3.1.1 Northern Hemisphere

Figure 1 shows that the July 1257 ensemble mean (solid blue line) is the only eruption scenario to lie consistently within 2σ of the tree-ring mean (grey band around the black line), with good agreement with tree-ring-reconstructed anomalies for both the timing and magnitude of peak cooling across the whole period (1257-1262). The January 1258 eruption ensemble mean (solid pink line) also results in peak cooling occurring in Summer 1258 although the magnitude of model-simulated cooling

205 is much greater (by over 1°C) than the peak tree-ring reconstructed cooling. Across individual January 1258 eruption ensembles (shown in Supplementary Document, Figure S2) only two lie within 2σ of the tree-ring mean for the whole period. By contrast for the individual July 1257 eruption ensembles seven lie within 2σ of the tree-ring mean for the whole period (Supplementary Document, Figure S3). Both July 1256 (dashed blue line) and January 1257 (dashed pink line) eruption scenarios result in peak cooling occurring a year early relative to the tree-ring-reconstructed mean and across both

210 scenarios no individual ensemble members lie within 2σ of the tree-ring mean for 1257-1260.
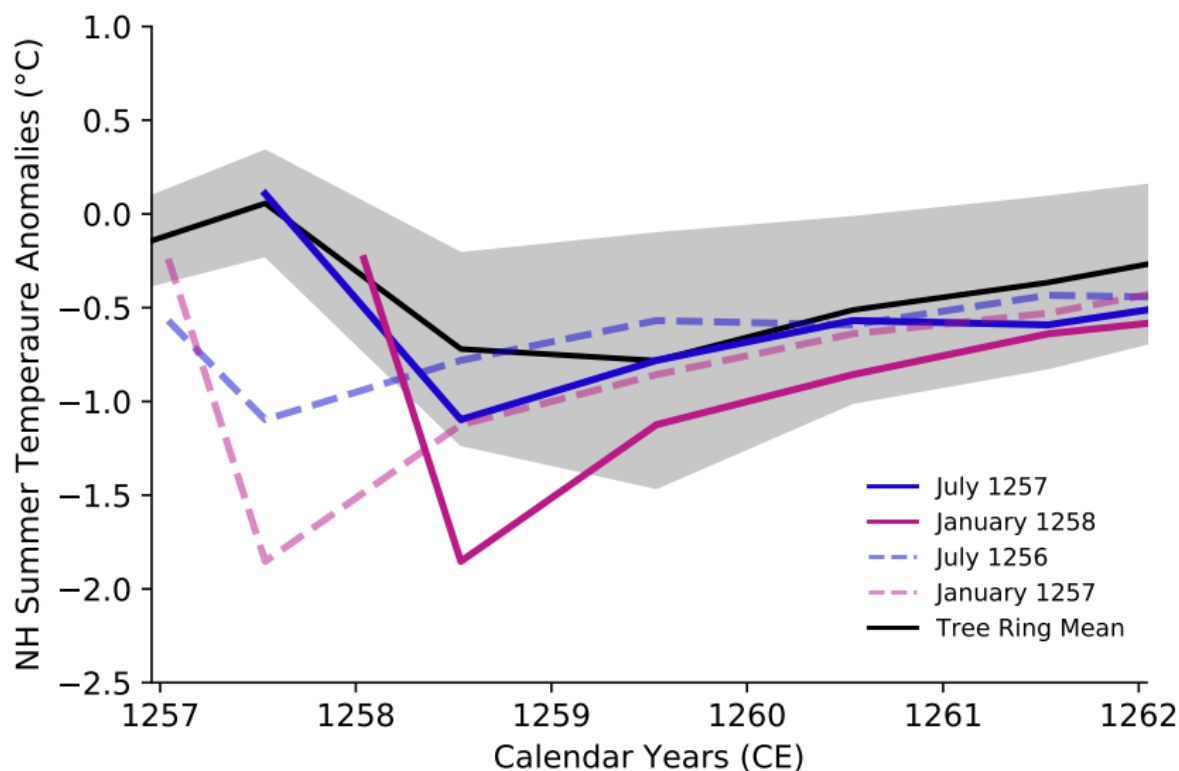
Figure 1. NH Summer June-July-August Surface temperature anomalies. Blue: July ensemble mean. Pink: January ensemble mean. Solid and dashed lines indicate different eruption years. Black line shows the mean of the tree-ring-reconstructed summer surface air temperature anomalies and grey band shows 2σ around the tree-ring mean. Tree-Ring data: Wilson et al., (2016), Schneider et al., (2015), Büntgen et al., (2021), Guillet et al., (2017). See Supplementary Sheet 2 for details of each tree-ring study.

When compared to the N-TREND spatially resolved tree-ring reconstructed anomalies (first column in Figure 2) the July 1257 ensemble mean (third column in Figure 2) results in more consistent agreement with the magnitude and spatial distribution of SAT anomalies across the NH for Summers 1258 and 1259. For Summer 1258 the mean grid point difference between N-TREND reconstructions and the July 1257 Ensemble mean is +0.19 (σ = 1.08) whilst the difference with the January 1258 Ensemble mean is +0.78 (σ = 0.99), with the January 1258 ensemble mean (second column in Figure 2) tending to overpredict summer SAT anomalies relative to N-TREND reconstructions. Across the US West Coast and Central and Northern Europe N-TREND reconstructions suggest cooling of -1°C to -2°C whereas model-simulated anomalies for the January 1258 ensemble mean are on the order of -2°C to -3°C. By contrast the July 1257 ensemble mean shows widespread but more moderate negative SAT anomalies of -1°C to -2°C across the NH for Summer 1258 and thus achieves better agreement with N-TREND reconstructions. Nonetheless, model-simulated anomalies for the July 1257 mean suggest cooling

of up to -2°C in Central and Northwest Asia which is an underprediction relative to N-TREND tree-ring reconstructions which suggest cooling of up to -3°C in Summer 1258.

230
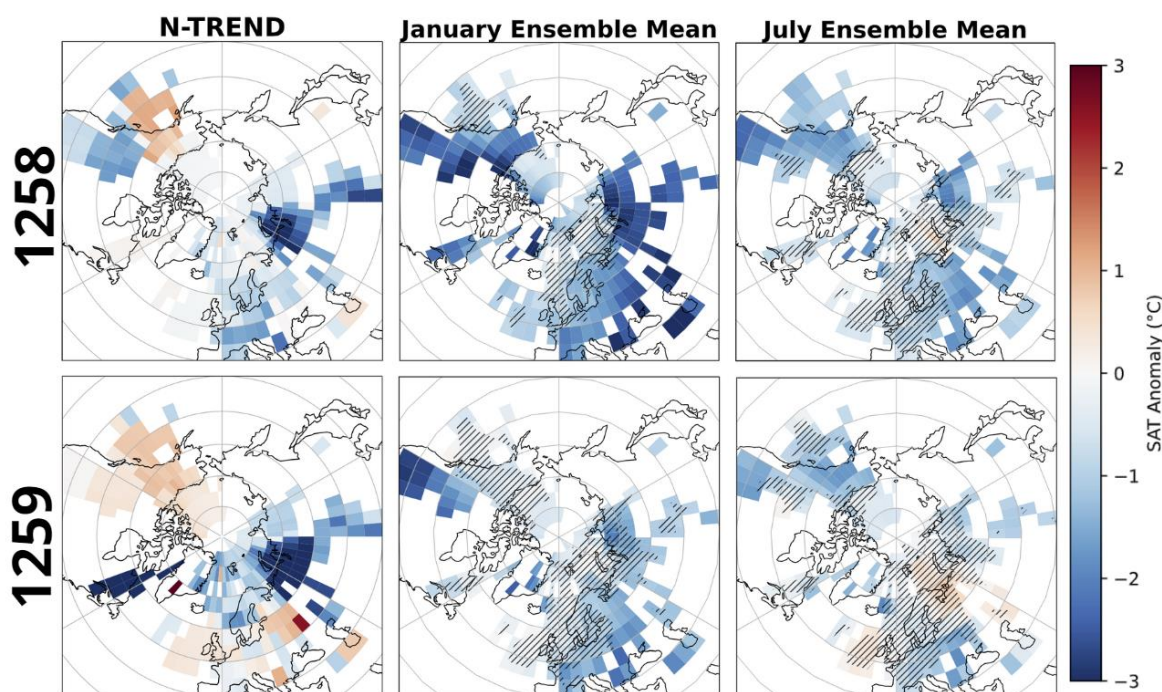
Figure 2. Spatially resolved N-TREND-Model comparison for June-July-August average 1258-59 for the Northern Hemisphere (40-90°N). N-TREND data from Anchukaitis et al., (2017). First column shows N-TREND reconstructed summer surface temperature anomalies. Second column shows model-simulated summer surface temperature
235 **anomalies for the January 1258 ensemble mean and third column shows the same for the July 1257 ensemble mean. Hashed areas show regions of less than 95% significance as determined using a grid box ANOVA analysis.**

Greater regional variability is seen in N-TREND SAT anomalies for summer 1259. N-TREND reconstructions suggest negative SAT anomalies in Northern Eurasia and Quebec of up to -3°C and between -1°C to -2°C in Northern Europe and
240 Central Asia. Positive SAT anomalies of up to +1°C are seen in Alaska and Western Europe. The January 1258 ensemble mean shows continued widespread negative anomalies of -1°C to -3°C across the whole NH and thus does not achieve consistent agreement with reconstructed anomalies across North and Western Europe, US West Coast or Alaska. By contrast, the July 1257 ensemble mean shows moderate positive SAT anomalies in Northern and Western Europe of up to +0.5°C although still somewhat under predicts the magnitude of cooling in Central and Northern Asia and the US East coast
245 relative to N-TREND reconstructions.

Notably neither the July 1257 or January 1258 ensemble mean achieves agreement with positive SAT anomalies reconstructed in Alaska for Summers 1258 and 1259. Across individual ensembles (See Supplementary Document, Figures S4-S7) only 1 July and 4 January ensembles show positive SAT anomalies in this region. Of these ensembles three are classified as having warm phase ENSO initial conditions. N-TREND reconstructions show moderate SAT anomalies in Alaska from 1255-56, with strong positive SAT anomalies first appearing in reconstructions for Summer 1257 (shown in Supplementary Document, Figure S8).

3.1.2 Globally Resolved Multi-Proxy Constraints

Multi-proxy-reconstructed SAT anomalies are shown in Figure 3 (top row) along with model-simulated SAT anomalies for a July 1257 eruption (second row) and a January 1258 eruption (third row) across Summers (JJA) 1258 (left) and 1259 (right). Overall, the July 1257 ensemble mean shows more consistent agreement with proxy SAT constraints across Europe, Asia, and North America, whilst the January 1258 ensemble mean tends to overpredict the magnitude of negative SAT anomalies relative to quantitative proxy constraints.

Summer 1258

For Summer 1258 large negative SAT anomalies are well constrained across Central Asia, with tree-ring reconstructions suggesting cooling in the region of up to -0.4°C in Tibet and -1.1°C in Mongolia (Xu et al., 2019, Davi et al., 2015, Davi et al., 2021) as well as the presence of frost rings late in the 1258 growth season (D'Arrigo et al., 2001). In Japan the Mirror of the East refers to persistent cold and wet conditions. Negative SAT anomalies are constrained across northern Russia, with cooling up -2.7°C (Briffa et al., 2013), and frost rings also present in the Polar Urals, Siberia (Hantemirov et al., 2004). Both January 1258 and July 1257 model ensembles suggest strong cooling across Central and Northern Asia, however, only the July 1257 ensemble mean lies consistently within +/-1°C of the proxy constraints whilst anomalies of up to -4°C for the January 1258 ensemble mean are an overprediction relative to proxy constraints (see filled symbols on Figures 3C and 3E).

Across Northern, Central, and Western Europe negative SAT anomalies are constrained by a combination of tree-ring reconstructions, with moderate cooling of up to -0.3°C in Europe (Büntgen et al., 2011), and a multitude of medieval chronicles across France, Germany, and England which refer to cold and wet conditions (Guillet et al., 2017). The July 1257 ensemble shows SAT anomalies of up to -1°C in good agreement with proxy constraints on the magnitude of cooling (see filled triangles across Europe in Figure 3C), whereas the January 1258 ensemble mean shows cooling between -2°C and -3°C. The Þorgils Saga Skarða in Iceland also refers to abnormally cold and wet weather during 1258 (Bierstedt, 2019) with ice core reconstructions in Greenland supporting moderate negative SAT anomalies of around -0.1°C (Guillet et al., 2017). January 1258 and July 1257 ensemble means suggest cooling of up to -3°C and -2°C respectively and so both overpredict the magnitude of cooling across Greenland.

280 SAT anomalies are more variable across North America with reconstructions in Eastern Canada showing both positive and negative SAT anomalies of 0.09°C and -1.6°C respectively (Gennaretti et al., 2014, Moore et al., 2001). The July 1257 ensemble shows agreement with both proxy constraints suggesting cooling of up to -2°C on Baffin Island and showing no significant SAT anomaly in the Quebec region, whilst the January 1258 ensemble mean shows cooling of up to -3°C and thus overpredicts cooling in both regions. Tree-ring reconstructions in the Western US and Canadian Rockies suggest

285 negative SAT anomalies of up to -0.5°C and -1.6°C (Martin et al., 2020, Luckman et al., 2005). The January 1258 ensemble overpredicts the magnitude of cooling relative to proxy constraints with SAT anomalies of up to -3°C whilst the July 1257 ensemble mean shows more moderate anomalies of up to -2°C. Positive SAT anomalies are well constrained by both lake sediment and tree-ring reconstructions in the Gulf of Alaska with warming of up to 0.1°C and 0.9°C (Loso, 2008, Wiles et al., 2014), however, neither January 1258 nor July 1257 ensemble means show positive SAT anomalies in this region.

290
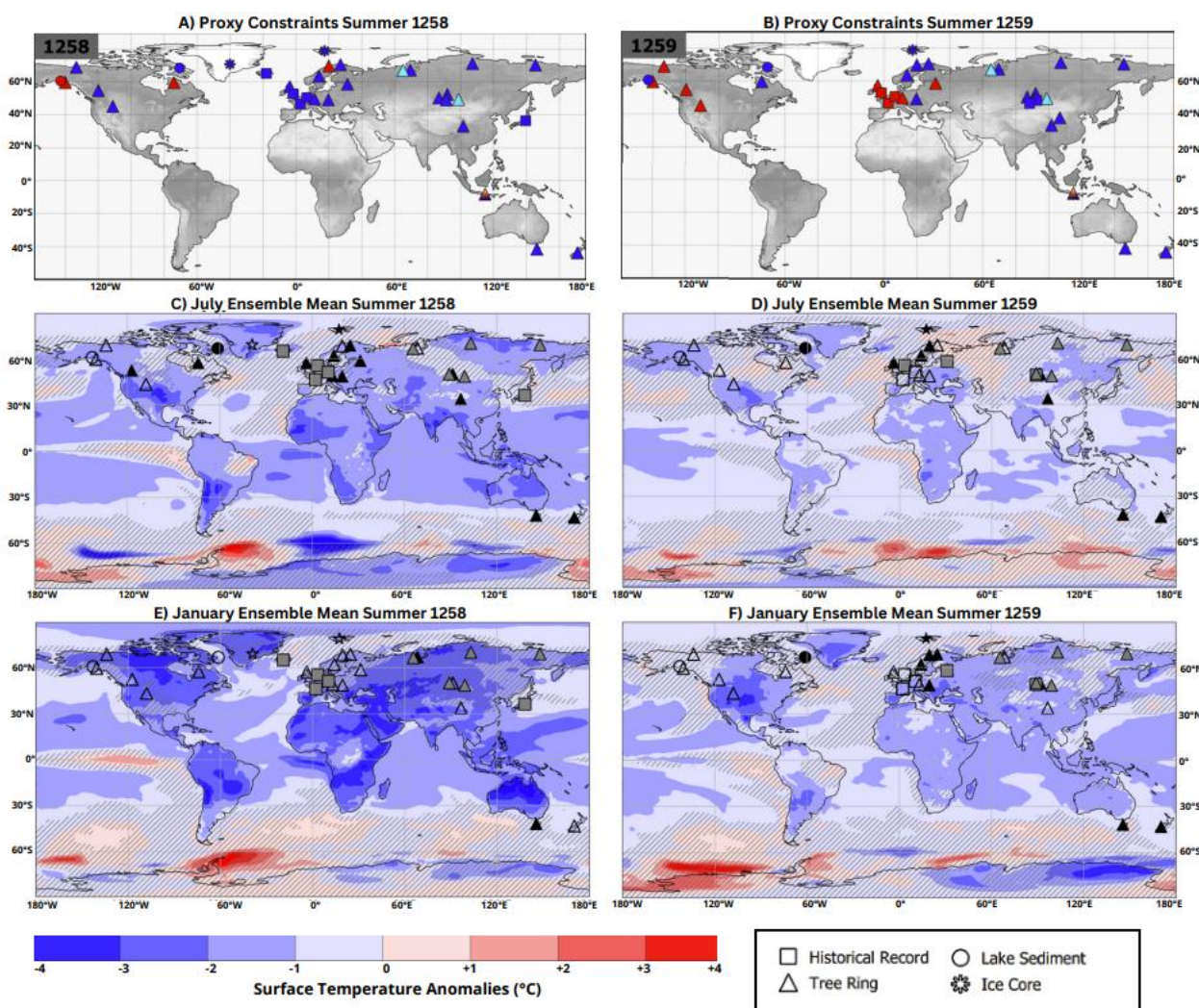
Figure 3: (a)-(b) Globally resolved multi-proxy database visualized for summers 1258 and 12-59. Symbols denote proxy data type, where blue/red shading denotes absolute negative or positive anomalies, respectively. (c)-(f) Globally resolved surface air temperature anomalies for summers (June-July-August) 1258 (left) and 1259 (right) for July 1257 eruptions (middle) and January 1258 eruptions (bottom) ensemble means. Surface air temperature anomalies were calculated relative to a 10-year background climatology constructed from the control ensemble mean. Hashed lines denote anomalies at <95% significance as determined by a grid point ANOVA analysis. Black filled symbols denote agreement within +/- 1°C between model-simulated anomalies and quantitative proxy records. Grey filled symbols denote agreement with qualitative proxy records.

Summer 1259

Persistent strong negative SAT anomalies are well constrained for Central Asia with tree-ring reconstructions suggesting continued cooling of up to -2.3°C in Mongolia and -0.3°C in Tibet (Davi et al., 2015, Xu et al., 2019) as well as frost rings present early in the 1259 growth season (Churakova et al., 2019, D'Arrigo et al., 2001). The Russian Chronicle of Novgorod refers to abnormal summer snowfall in the Altai mountains and unusual summer frost days (Stothers, 2000, Borisenkov and Pasetsky, 1988) with tree-ring reconstructions showing continued negative SAT anomalies across Northern Russia of up to -4°C (Briffa et al., 2013). Both January 1258 and July 1257 ensemble means show moderate negative anomalies of between -1°C and -2°C in Central Asia, however, only the January 1258 ensemble mean shows stronger negative SAT anomalies of up to -3°C in Northern Russia whilst anomalies for the July 1257 ensemble mean do not exceed 95% significance. Tree-ring reconstructions show some positive SAT anomalies across Central Europe of up to 0.2°C (Büntgen et al., 2011) and in Western Europe medieval chronicles refer to a hot and dry summer (Guillet et al., 2017). Very moderate SAT anomalies across Europe are only shown by the July 1257 ensemble mean, whilst the January 1258 ensemble continues to show cooling in the region of up to -2°C.

Negative SAT anomalies persist across Eastern North America with cooling of up to -2.6°C and -1.6°C constrained from tree-ring and lake sediment reconstructions respectively (Gennaretti et al., 2014, Moore et al., 2001). Cooling of up to -2°C is shown by both ensemble means across Baffin Island (NE Canada), however, neither ensemble achieves agreement with the stronger cooling signal in Quebec. Along the Western coast of North America tree-ring reconstructions yield positive SAT anomalies of up to +0.8°C in the Missouri River Basin and +0.3°C in the Canadian Rockies (Martin et al., 2020, Luckman et al., 2005). Both ensembles continue to show cooling along the US West Coast although the magnitude is more moderate for the July 1257 ensemble. In the Gulf of Alaska there is some discrepancy as tree-ring reconstructions suggest continued positive SAT anomalies of up to +0.7°C whilst lake sediment reconstructions suggest moderate negative SAT anomalies of up to -0.1°C (Loso, 2008, Wiles et al., 2014). The January 1258 ensemble mean shows no anomalies exceeding 95% significance in Alaska whilst the July 1257 ensemble mean shows continued cooling of up to -2°C and so neither eruption scenario achieves good agreement with proxy constraints.

3.2 Re-evaluating Evidence for a January 1258 Eruption Date

Two lines of evidence have previously been invoked for a January 1258 eruption date: references in medieval chronicles to a "dark lunar eclipse" in mid-May 1258 (Stothers, 2000) and peak sulfate fall out in Greenland Ice Cores in early 1259 (Zielinski et al., 1994). Figure 4a shows model-simulated Stratospheric Aerosol Optical Depth (SAOD) averaged across

330   western Europe for the years following the eruption. Marked by the grey lines are the dark lunar eclipses of May 1258 and Nov 1258 identified by Stothers (2000) in the Bury Saint Edmunds Abbey chronicle and Guillet et al., (2017) in the Annales Ianuenses respectively, where for the moon to appear dark an SAOD > 0.1 is needed (Stothers, 2000). Whilst a January 1258 eruption scenario does result in a later SAOD peak, both a July 1257 and a January 1258 eruption result in SAOD >> 0.1 during both May and November 1258 and therefore either eruption scenario could account for observations of darkened

335   lunar eclipses.
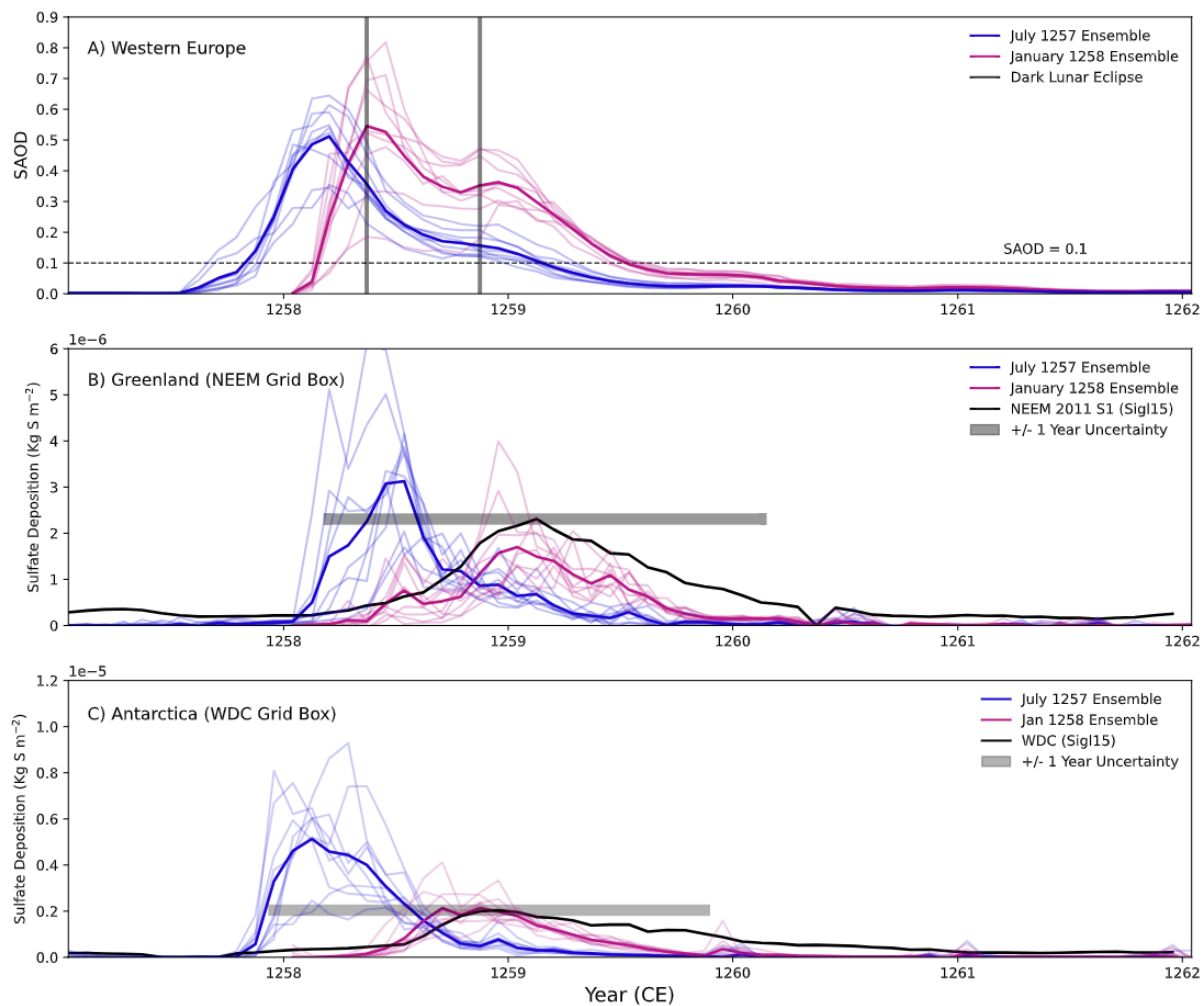
Figure 4: A) Model-simulated Stratospheric Aerosol Optical Depth (SAOD) timeseries averaged across Western Europe (Lat: 40-60°N, Longitude: 10W-10°E) for July 1257 (blue line) and Jan 1258 (pink line) eruption scenarios where bold lines are the ensemble means. Vertical grey bars denote historical records of dark lunar eclipses in May 1258 (England) and November 1258 (Genoa). The dashed horizontal line at SAOD = 0.1 denotes the minimum SAOD required for a dark lunar eclipse. B-C) Model-simulated sulfate deposition (kg S m-2) over Greenland and Antarctica ice sheets for July 1257 (Blue) and January 1258 (Pink) eruption scenarios. The region of deposition is limited to the single model grid box containing NEEM (Greenland) and WDC (Antarctica) ice core drill sites respectively. Black lines are timeseries from NEEM and WDC ice core records respectively (Sigl et al., 2015) with grey bars showing +/- 1-year uncertainty for the timing of peak deposition.

Figures 4B and 4C show model-simulated sulfate deposition across Greenland and Antarctic ice sheets at the single grid-boxes containing WDC and NEEM ice cores respectively, for July 1257 and January 1258 eruption scenarios. Additional sulfate deposition timeseries are derived from NEEM and WDC ice cores respectively (Sigl et al 2015). See Supplementary Figure S10 for ice sheet-averaged model-simulated sulfate deposition across Greenland and Antarctica. The July 1257 ensemble shows peak deposition occurring in early to mid-1258, whilst the January 1258 ensemble shows peak deposition in early 1259, which is in better alignment with Greenland and Antarctic ice core records. Nonetheless, the resolution of the ice core age uncertainty (+/- 1 year as shown by the grey shading) of the timing of peak deposition is less than the 6-month offset between model-simulated deposition timeseries, meaning these ice core constraints cannot robustly distinguish the difference in timing of peak deposition between eruption scenarios. Moreover, although the magnitude of deposition for the January 1258 ensemble mean is most comparable to the ice core records, particularly in Antarctica, across both eruption scenarios there are individual ensembles which show agreement with the magnitude of peak deposition within the grid boxes containing the WDC and NEEM ice core records.

4. Discussion

4.1 Constraining the Eruption Year and Season of the Mt. Samalas eruption

As shown in Figure 1, both July 1256 and January 1257 eruption scenarios result in peak surface cooling occurring a year too early relative to reconstructed SAT anomalies. Thus, an early eruption date such as Spring 1256, as proposed by Bauch (2019), is unfeasible for the Mt. Samalas eruption. Across the two remaining eruption scenarios only the July 1257 eruption ensemble lies consistently within 2σ of the tree ring-reconstructed mean between 1258-1262. By contrast, the January 1258 eruption ensemble results in peak cooling being over 1°C greater than tree ring reconstructions for Summer 1258.

When compared with spatially resolved N-TREND reconstructions model-simulated SAT anomalies for the January ensemble mean continue to consistently overpredict the magnitude of cooling for both 1258 and 1259 across the NH. Whilst

the spatial agreement of SAT anomalies for the July 1257 ensemble mean does not precisely replicate those reconstructed
from the N-TREND tree ring record it does show widespread but less extreme negative SAT anomalies across the NH and
thus achieves better agreement with reconstructed anomalies on a regional basis. This is confirmed by comparison between
globally resolved model-simulated ensemble mean SAT anomalies and multi-proxy-reconstructed anomalies where the
January 1258 ensemble mean consistently over predicts the magnitude of cooling in key regions across Europe, Central Asia,
and the US, whilst the July 1257 ensemble mean results in better agreement across these regions with more moderate
negative SAT anomalies.

A re-evaluation of evidence for a January 1258 eruption finds that a Summer 1257 eruption can satisfy constraints from both
ice core records and historically documented dark lunar eclipses. Simulated ice sheet sulfate deposition show that for
eruption scenarios 6 months apart there is a distinguishable off-set in the timing and magnitude of deposition, with the bi-
polar ratio between northern and southern hemisphere ice sheets varying depending on eruption season. Nonetheless, these
ice core sulfate records currently have insufficient resolution to discriminate between January and July eruption scenarios for
the Mt. Samalas eruption with implications for VSSI estimates (see Section 4.3).

Overall, the multi-proxy to model comparison utilized in this study provides a clear distinction between July 1257 and
January 1258 eruption scenarios in both the magnitude and spatial distribution of SAT anomalies. The better agreement
between proxy reconstructions and model-simulated anomalies for a July 1257 eruption provides strong support for a
Summer 1257 date for the Mt. Samalas eruption.

4.2 Regionally Heterogenous Climate Response

Multi-Proxy SAT reconstructions highlight the regionally heterogenous climate response following the Mt. Samalas
eruption. The largest negative SAT anomalies occur across Central Asia and Northern Russia, with cooling of -2°C to -4°C
between 1258 and 1259, making these as some of the most severely impacted regions in the NH. The role of sudden and
severe cooling associated with the Mt. Samalas eruption in the decline of the Mongol Empire is therefore plausible (Kern et
al., 2021). Alongside references to extreme and abnormal weather conditions, the Azuma Kagami in Japan also highlights
the severity of the Shôga famine between 1257-60 (Farris, 2006). Model-simulated cooling of up to -1°C across Japan
suggest the severity of this famine could have been amplified by the climate response to the Mt. Samalas eruption in 1258-
59. Similar evidence exists in the Middle East with famine and pestilence reported across Syria, Iraq, and Southern Turkey in
1258 (Stothers, 2000). A model-simulated July 1257 eruption scenario suggests cooling of up to -2°C in the region and thus
supports a possible association with the Mt. Samalas eruption. Reconstructed and model-simulated SAT anomalies suggest
less severe cooling across Europe for 1258 (<-1°C) and relative warming in the region for 1259. Nonetheless, this is still
associated with significant economic and social disturbances, with historical records reporting famine and social unrest
(Guillet et al., 2017, Stothers, 2000).

Büntgen et al., (2022) find negative TRW growth anomalies along the US West Coast for Summer 1257 and suggest this is evidence for the onset of climate perturbations in the NH before the end of the 1257 growth season and for a Summer 1257

405   eruption date. Model-simulated anomalies for a July 1257 eruption, however, show no significant anomalies occurring across the US or NH during Summer 1257 (see Supplementary Document, Figure S9). Instead, model-simulated SAT anomalies for a July 1257 eruption only show significant negative SAT anomalies across South America, Africa, and Oceania beginning in Late Summer 1257 with cooling in some regions of up to -2°C. Such extreme sudden cooling would be expected to have significant, but as yet unknown, consequences for communities and civilizations in the Southern Hemisphere. For example,

410   the first settlement of New Zealand most likely occurred between 1250–1275, with suggestions this may have reflected a climate-induced migration associated at least in part with the impacts of the Mt. Samalas eruption (Anderson, 2016, Bunbury et al., 2022). Apart from recent analysis of the localized impacts and recovery following the Mt. Samalas eruption (Malawani et al., 2022) the general sparsity of currently available proxy data across the SH precludes definitive conclusions as to climate and social response in the SH following the Mt. Samalas eruption.

415

Notably, neither the January 1258 or July 1257 ensemble mean replicates reconstructed positive SAT anomalies in Alaska for Summer 1258 or the wider US west coast for Summer 1259. Across individual eruption ensembles only 5 show positive SAT anomalies in this region and of these ensembles 3 are classified as having warm phase ENSO initial conditions. N-TREND spatially resolved reconstructions show positive SAT anomalies over Alaska from Summer 1257-59, with warm

420   phase El Niño-like conditions during this period being supported by positive tree ring-reconstructed temperature anomalies in Alaska (Guillet et al., 2017) and the muted absolute temperature signal seen in $\delta^{18}O$ coral reconstructions from the central tropical Pacific (most likely explained by the superposition of a volcanic cooling signal and a warm El Niño-like signal (Dee et al. 2020, Robock 2020)). The role of volcanic eruptions in perturbing ENSO remains debated (Mann et al. 2005, Stevenson et al. 2018, Dee et al. 2020, Robock 2020) although climate simulations and proxy records suggest an increased

425   probability for the occurrence of an El Niño event in the first or second year after a large volcanic eruption (see McGregor et al 2020 for a full review). El Niño-like warm conditions may therefore have prevailed at the time of the Mt. Samalas eruption with subsequent volcano-ENSO interactions potentially acting to enhance these pre-existing El Niño-like conditions.

4.3 Model and Proxy Limitations

430   The January 1258 ensemble mean consistently over-predicts the magnitude of cooling relative to proxy-reconstructed anomalies by around 1°C. As such a January 1258 eruption data can only be considered feasible if proxy-reconstructions are thought to under-record the magnitude of cooling following large eruptions. The possible effect of chronological errors resulting from missing growth rings due to extreme cooling following large eruptions has been highlighted (Mann et al., 2012), as well as the need to correct tree ring reconstructions for the effect of increased diffuse light due to enhanced

435   scattering (Robock, 2005). Lücke et al., (2019) also highlight the importance of accounting for biologically based memory effects, which can lead to dampening of volcanic cooling signals especially in ring width-based chronologies. Nonetheless, tree-ring data has been shown to record extreme cooling events synchronous with evidence for explosive volcanic eruptions over the last two millennia without chronological errors (Stoffel et al., 2015) and in good agreement with instrumental observations following large eruptions (Esper et al., 2013), where the inclusion of maximum latewood density (MXD) data

440   has reduced attenuation of the volcanic cooling signal (Esper et al., 2014, Stoffel et al., 2015).

Alternatively, model-simulated anomalies may be overpredicting the magnitude of cooling following large volcanic eruptions. Timmreck et al., (2009) highlighted the strong dependence of model-simulated post-eruption climate responses following large volcanic eruptions on the aerosol particle size distribution due to self-limiting effects of larger particles

445   (Pinto et al., 1989). Particle characteristics are difficult to constrain retrospectively for historic eruptions such as Mt. Samalas and thus represent one of the most significant uncertainties with modelling historic eruptions, nonetheless, processes such as particle coagulation are accounted for by the aerosol microphysics scheme applied in model simulations for this study. There is also uncertainty as to the VSSI, which could have been overestimated in our simulations. Injection height was also held constant, also a key parameter in modulating the post-eruption climate response (Robock, 2000, Stoffel et al., 2015). The

450   values chosen for the SO_2 emission and injection height are consistent with current best estimates for the Mt. Samalas eruption although there remains uncertainty as to their exact values. Stoffel et al., (2015) found that increasing plume height from 22-26 km to 33-36 km increased the magnitude of the peak post-eruption NH JJA temperature anomaly to -4°C for a January eruption and -1°C and -2°C for May and July eruption scenarios respectively. A higher plume height than the 20km used in our study would therefore likely further enforce our central conclusion that better agreement between proxy and

455   model temperature anomalies is achieved for a summer 1257 eruption date, whilst a greater plume height for a January 1258 eruption would only further overpredict the magnitude of post-eruption cooling.

Proxy records able to reconstruct hydroclimate anomalies (such as stalagmite and tree ring records) were investigated as additional constraints in our study (See Supplementary Figures S11 and S12), although most lacked the annual resolution

460   required for direct comparison to model outputs. Previous studies utilizing tree-ring reconstructed hydroclimate anomalies have suggested moderately wetter conditions in the SH during 1258, potentially indicative of a southward ITCZ shift (Tejedor et al., 2021, Büntgen et al., 2022). Nonetheless, without a greater distribution of annually resolved proxy records able to reconstruct tropical hydroclimate anomalies, definitive conclusions as to the ITCZ and global hydroclimate response following the Mt. Samalas eruption remain elusive.

465

Model-simulated ice sheet sulfate deposition (Fig. 4) shows a clear distinction between January and July eruption scenarios in both the timing and hemispheric distribution of deposition. For the same stratospheric SO_2 injection, an eruption during NH summer results in more pronounced asymmetric polar deposition, with the magnitude of peak deposition in Antarctica

(see Supplementary Figure S10) being nearly a factor of 3x greater than for an eruption during the SH summer, likely due to the stronger branch of the Brewer-Dobson circulation and seasonal effects on aerosol transport and depositional processes. This highlights that for a given deposition there is the potential for non-unique VSSI estimates depending on the season of eruption. As such, this represents an uncertainty when reconstructing VSSI from ice core sulfate deposition for eruptions such as Mt. Samalas where the season of eruption is unconstrained (Marshall et al., 2021). Moreover, the +/-1 year age uncertainty of the NEEM and WDC ice core records (Sigl et al., 2015) meant they were unable to clearly distinguish between January and July eruption scenarios thus suggests that, at least until higher temporal resolution is possible in ice core records, they are an unsuitable tool to constrain eruption season for Common Era eruptions such as Mt. Samalas.

5 Conclusions

We have utilized eighteen aerosol-climate UKESM1 ensemble simulations for the 1257 Mt. Samalas eruption in combination with the most complete globally resolved multi-proxy database to date for the Mt. Samalas eruption. This allowed more precise constraints on the year and season as well as the regionally heterogeneous climate response following the Mt. Samalas eruption. Comparison with NH averaged and spatially resolved tree ring reconstructions showed that a Summer 1257 eruption scenario agrees best with reconstructed SAT anomalies, with a January 1258 eruption consistently over predicting the magnitude of cooling relative to reconstructions. The regionally variable SAT response following the eruption is revealed by multi-proxy reconstructions which lend support to inferred social, economic and historical consequences across Europe and Asia following the eruption. Model-simulated SAT anomalies also suggest the onset of sudden a severe cooling across the SH, with the potential for significant social and economic consequences in impacted communities across South America, Africa, and Oceania. The spatial distribution of SAT anomalies shows some sensitivity to initial atmospheric-ocean conditions, with positive SAT anomalies in Alaska being potentially indicative of warm El Niño-like conditions at the time of the eruption, with potential ENSO-Volcano interactions enhancing these conditions further.

Overall, the proxy to model comparison employed in this study has been shown as an effective approach to constrain uncertain eruption source parameters. This framework therefore has significant potential in similar applications to constrain unknown initial conditions and regional climatic impacts for other historic eruptions with sufficient concurrent proxy evidence. A greater global distribution of proxy evidence, especially in the Southern Hemisphere where all types of proxy evidence are sparse, will strengthen this proxy-model framework approach for future analysis. The incorporation of hydroclimate anomalies in particular has the potential to add further independent constraints, although relies on the development of higher resolution records, especially at low latitude sites. A re-evaluation of the application of the use of ice core sulfate records to estimate eruption season and VSSI also highlights current limitations in the approach. This is due to insufficient seasonal resolution in ice core records and seasonal effects on global aerosol distribution which in our

simulations results in different deposition signatures (e.g. in the timing, peak deposition, and total magnitude) for each season for the same VSSI.

505 Finally, both proxy-reconstructed and model-simulated temperature anomalies highlight the severity of the global climate response following a large tropical explosive eruption, with historical records confirming widespread and severe economic and social consequences. This adds further weight to recent calls (Cassidy and Mani, 2022) for increased global preparedness for the next large magnitude explosive volcanic eruption, given profound global consequences that would be expected, as clearly demonstrated by the Mt. Samalas eruption.

510 **Data Availability**

Summary model output is currently being uploaded to the CEDA archive.

Supplement

The supplement related to this article is available online at:

515

Author Contributions

LW, LM, and AS jointly conceived the project methodology. LM ran the UKESM model simulations. LW performed the analysis, visualisation, and writing of the manuscript with supervision from LM and AS. All authors jointly reviewed and 520 edited the paper.

Competing Interests

The authors declare that they have no conflict of interest.

525 **Acknowledgements**

This research formed part of LWs MSci Thesis at the University of Cambridge. LW would like to thank O. Shorttle and E. Harper for their additional supervision and encouragement throughout this project, as well as Newnham College for supporting the presentation of this work through a travel bursary. LM and AS acknowledge support from NERC grant NE/S000887/1 (VOL-CLIM), and AS additionally acknowledges funding from NERC grant NE/S00436X/1 (V-PLUS). The 530 authors would also like to thank M. Sigl and K. Anchukaitis for providing ice core and tree ring data sets utilized in this project, and N.L Abraham for technical modelling support. This work used the ARCHER UK National Supercomputing Service (http://www.archer.ac.uk) and JASMIN, the UK collaborative data analysis facility.

Financial Support

535 This research was supported by NERC grant NE/S000887/1 (VOL-CLIM) and NERC grant NE/S00436X/1 (V-PLUS).

References

Anchukaitis, K.J., Wilson, R., Briffa, K.R., Büntgen, U., Cook, E.R., D'Arrigo, R., Davi, N., Esper, J., Frank, D., Gunnarson, B.E., Hegerl, G., Helama, S., Klesse, S., Krusic, P.J., Linderholm, H.W., Myglan, V., Osborn, T.J., Zhang, P., Rydval, M. and Schneider, L. (2017). Last millennium Northern Hemisphere summer temperatures from tree rings: Part II,
540 spatially resolved reconstructions. Quaternary Science Reviews, [online] 163, pp.1–22. doi:10.1016/j.quascirev.2017.02.020.

Anderson, A. The first migration : Māori origins 3000BC - AD1450. Wellington, New Zealand: Bridget Williams Books. Doi: 10.7810/9780947492793, 2016.

545 Archibald, A.T., O'Connor, F.M., Abraham, N.L., Archer-Nicholls, S., Chipperfield, M.P., Dalvi, M., Folberth, G.A., Dennison, F., Dhomse, S.S., Griffiths, P.T., Hardacre, C., Hewitt, A.J., Hill, R.S., Johnson, C.E., Keeble, J., Köhler, M.O., Morgenstern, O., Mulcahy, J.P., Ordóñez, C. and Pope, R.J. (2020). Description and evaluation of the UKCA stratosphere–troposphere chemistry scheme (StratTrop vn 1.0) implemented in UKESM1. Geoscientific Model Development, 13(3), pp.1223–1266. doi:10.5194/gmd-13-1223-2020.
550

Bauch, M. (2019). Chronology and impact of a global moment in the 13th century. In: The Dance of Death in Late Medieval and Renaissance Europe. Routledge. ISBN 9781032083391

Bierstedt, A. (2019). Weather and Ideology in Íslendinga saga A Case Study of the Volcanic Climate Forcing of the 1257
555 Samalas eruption. M.A. thesis, University of Iceland

Borisenkov, Y.P. and Pasetsky, V.M., 1988. Millennium-Long Chronicle of Unusual Natural Events. Misl', Moscow.

Broccoli, A.J., Dahl, K.A. and Stouffer, R.J. (2006). Response of the ITCZ to Northern Hemisphere cooling. Geophysical
560 Research Letters, 33(1), p.n/a-n/a. doi:10.1029/2005gl024546.

Bunbury, M.M.E., Petchey, F. and Bickler, S.H. (2022). A new chronology for the Māori settlement of Aotearoa (NZ) and the potential role of climate change in demographic developments. Proceedings of the National Academy of Sciences, [online] 119(46). doi:10.1073/pnas.2207609119.
565

Büntgen, U., Allen, K., Anchukaitis, K.J., Arseneault, D., Boucher, É., Bräuning, A., Chatterjee, S., Cherubini, P., Churakova (Sidorova), O.V., Corona, C., Gennaretti, F., Grießinger, J., Guillet, S., Guiot, J., Gunnarson, B., Helama, S., Hochreuther, P., Hughes, M.K., Huybers, P. and Kirdyanov, A.V. (2021). The influence of decision-making in tree ring-based climate reconstructions. Nature Communications, [online] 12(1), p.3411. doi:10.1038/s41467-021-23627-6.
570

Büntgen, U., Kyncl, T., Ginzler, C., Jacks, D.S., Esper, J., Tegel, W., Heussner, K.-U. and Kyncl, J. (2013). Filling the Eastern European gap in millennium-long temperature reconstructions. Proceedings of the National Academy of Sciences, 110(5), pp.1773–1778. doi:10.1073/pnas.1211485110.

575 Büntgen, U., Smith, S.H., Wagner, S., Krusic, P., Esper, J., Piermattei, A., Crivellaro, A., Reinig, F., Tegel, W., Kirdyanov, A., Trnka, M. and Oppenheimer, C. (2022). Global tree-ring response and inferred climate variation following the mid-thirteenth century Samalas eruption. Climate Dynamics, 59(1-2), pp.531–546. doi:10.1007/s00382-022-06141-3.

Buntgen, U., Tegel, W., Nicolussi, K., McCormick, M., Frank, D., Trouet, V., Kaplan, J.O., Herzig, F., Heussner, K.-U. .,
580 Wanner, H., Luterbacher, J. and Esper, J. (2011). 2500 Years of European Climate Variability and Human Susceptibility. Science, 331(6017), pp.578–582. doi:10.1126/science.1197175.

Campbell, B.M.S. (2017). Global climates, the 1257 mega-eruption of Samalas volcano, Indonesia, and the English food crisis of 1258. Transactions of the Royal Historical Society, 27, pp.87–121. doi:10.1017/s0080440117000056.

585

Cassidy, M. and Mani, L. (2022). Huge volcanic eruptions: time to prepare. Nature, [online] 608(7923), pp.469–471. doi:10.1038/d41586-022-02177-x.

Davi, N.K., D'Arrigo, R., Jacoby, G.C., Cook, E.R., Anchukaitis, K.J., Nachin, B., Rao, M.P. and Leland, C. (2015). A long-
590 term context (931–2005 C.E.) for rapid warming over Central Asia. Quaternary Science Reviews, 121, pp.89–97. doi:10.1016/j.quascirev.2015.05.020.

Davi, N.K., Rao, M.P., Wilson, R., Andreu-Hayles, L., Oelkers, R., D'Arrigo, R., Nachin, B., Buckley, B., Pederson, N., Leland, C. and Suran, B. (2021). Accelerated Recent Warming and Temperature Variability Over the Past Eight Centuries in
595 the Central Asian Altai From Blue Intensity in Tree Rings. Geophysical Research Letters, [online] 48(16). doi:10.1029/2021gl092933.

Dee, S.G., Cobb, K.M., Emile-Geay, J., Ault, T.R., Edwards, R.L., Cheng, H. and Charles, C.D. (2020). No consistent ENSO response to volcanic forcing over the last millennium. Science, [online] 367(6485), pp.1477–1481.
600 doi:10.1126/science.aax2000.

Divine, D., Isaksson, E., Martma, T., Meijer, H.A.J., Moore, J., Pohjola, V., van de Wal, R.S.W. and Godtliebsen, F. (2011). Thousand years of winter surface air temperature variations in Svalbard and northern Norway reconstructed from ice-core data. Polar Research, 30(1), p.7379. doi:10.3402/polar.v30i0.7379.
605

Esper, J., Düthorn, E., Krusic, P.J., Timonen, M. and Büntgen, U. (2014). Northern European summer temperature variations over the Common Era from integrated tree-ring density records. Journal of Quaternary Science, 29(5), pp.487–494. doi:10.1002/jqs.2726.

610 Esper, J., George, S.St., Anchukaitis, K., D'Arrigo, R., Ljungqvist, F.C., Luterbacher, J., Schneider, L., Stoffel, M., Wilson, R. and Büntgen, U. (2018). Large-scale, millennial-length temperature reconstructions from tree-rings. Dendrochronologia, [online] 50, pp.81–90. doi:10.1016/j.dendro.2018.06.001.

Fell, H.G., Baldini, J.U.L., Dodds, B. and Sharples, G.J. (2020). Volcanism and global plague pandemics: Towards an
615 interdisciplinary synthesis. Journal of Historical Geography, [online] 70, pp.36–46. doi:10.1016/j.jhg.2020.10.001.

Gennaretti, F., Arseneault, D., Nicault, A., Perreault, L. and Begin, Y. (2014). Volcano-induced regime shifts in millennial tree-ring chronologies from northeastern North America. Proceedings of the National Academy of Sciences, 111(28), pp.10077–10082. doi:10.1073/pnas.1324220111.
620

Guillet, S., Corona, C., Stoffel, M., Khodri, M., Lavigne, F., Ortega, P., Eckert, N., Sielenou, P.D., Daux, V., Churakova (Sidorova), Olga V., Davi, N., Edouard, J.-L., Zhang, Y., Luckman, Brian H., Myglan, V.S., Guiot, J., Beniston, M., Masson-Delmotte, V. and Oppenheimer, C. (2017). Climate response to the Samalas volcanic eruption in 1257 revealed by proxy records. Nature Geoscience, 10(2), pp.123–128. doi:10.1038/ngeo2875.
625

Helama, S., Huhtamaa, H., Verkasalo, E. and Läänelaid, A. (2017). Something old, something new, something borrowed: New insights to human-environment interaction in medieval Novgorod inferred from tree rings. Journal of Archaeological Science: Reports, 13, pp.341–350. doi:10.1016/j.jasrep.2017.04.008.

630 Kern, Z., Pow, S., Pinke, Z. and Ferenczi, L. (2021). Samalas and the Fall of the Mongol Empire: A volcanic eruption's influence on the dissolution of history's largest contiguous empire. EGU General Assembly. doi:10.5194/egusphere-egu21-3460.

Lavigne, F., Degeai, J.-P. ., Komorowski, J.-C. ., Guillet, S., Robert, V., Lahitte, P., Oppenheimer, C., Stoffel, M., Vidal,
635 C.M., Surono, Pratomo, I., Wassmer, P., Hajdas, I., Hadmoko, D.S. and de Belizal, E. (2013). Source of the great A.D. 1257 mystery eruption unveiled, Samalas volcano, Rinjani Volcanic Complex, Indonesia. Proceedings of the National Academy of Sciences, 110(42), pp.16742–16747. doi:10.1073/pnas.1307520110.

Loso, M.G. (2008). Summer temperatures during the Medieval Warm Period and Little Ice Age inferred from varved
640 proglacial lake sediments in southern Alaska. Journal of Paleolimnology, 41(1), pp.117–128. doi:10.1007/s10933-008-9264-9.

Lücke, L.J., Hegerl, G.C., Schurer, A.P. and Wilson, R. (2019). Effects of Memory Biases on Variability of Temperature Reconstructions. Journal of Climate, [online] 32(24), pp.8713–8731. doi:10.1175/jcli-d-19-0184.1.

645

Luckman, B.H. and Wilson, R.J.S. (2005). Summer temperatures in the Canadian Rockies during the last millennium: a revised record. Climate Dynamics, 24(2-3), pp.131–144. doi:10.1007/s00382-004-0511-0.

Malawani, M.N., Lavigne, F., Sastrawan, W.J., Jamaluddin, Sirulhaq, A. and Hadmoko, D.S. (2022). The 1257 CE
650 cataclysmic eruption of Samalas volcano (Indonesia) revealed by indigenous written sources: Forgotten kingdoms, emergency response, and societal recovery. Journal of Volcanology and Geothermal Research, [online] 432, p.107688. doi:10.1016/j.jvolgeores.2022.107688.

Mann, M.E., Cane, M.A., Zebiak, S.E. and Clement, A. (2005). Volcanic and Solar Forcing of the Tropical Pacific over the
655 Past 1000 Years. Journal of Climate, [online] 18(3), pp.447–456. doi:10.1175/jcli-3276.1.

Mann, M.E., Fuentes, J.D. and Rutherford, S. (2012). Underestimation of volcanic cooling in tree-ring-based reconstructions of hemispheric temperatures. Nature Geoscience, 5(3), pp.202–205. doi:10.1038/ngeo1394.

660 Marshall, L.R., Schmidt, A., Johnson, J.S., Mann, G.W., Lee, L.A., Rigby, R. and Carslaw, K.S. (2021). Unknown Eruption Source Parameters Cause Large Uncertainty in Historical Volcanic Radiative Forcing Reconstructions. Journal of Geophysical Research: Atmospheres, [online] 126(13). doi:10.1029/2020jd033578.

Martin, J.T., Pederson, G.T., Woodhouse, C.A., Cook, E.R., McCabe, G.J., Anchukaitis, K.J., Wise, E.K., Erger, P.J., Dolan,
665 L., McGuire, M., Gangopadhyay, S., Chase, K.J., Littell, J.S., Gray, S.T., George, S.S., Friedman, J.M., Sauchyn, D.J., St-Jacques, J.-M. and King, J. (2020). Increased drought severity tracks warming in the United States' largest river basin. Proceedings of the National Academy of Sciences, [online] 117(21), pp.11328–11336. doi:10.1073/pnas.1916208117.

McCarroll, D., Loader, N.J., Jalkanen, R., Gagen, M.H., Grudd, H., Gunnarson, B.E., Kirchhefer, A.J., Friedrich, M.,
670 Linderholm, H.W., Lindholm, M., Boettger, T., Los, S.O., Remmele, S., Kononov, Y.M., Yamazaki, Y.H., Young, G.H. and Zorita, E. (2013). A 1200-year multiproxy record of tree growth and summer temperature at the northern pine forest limit of Europe. The Holocene, 23(4), pp.471–484. doi:10.1177/0959683612467483.

McGregor, S., Khodri, M., Maher, N., Ohba, M., Pausata, F.S.R. and Stevenson, S. (2020). The Effect of Strong Volcanic
675 Eruptions on ENSO. Geophysical Monograph Series, [online] pp.267–287. doi:10.1002/9781119548164.ch12.

Melvin, T.M., Grudd, H. and Briffa, K.R. (2012). Potential bias in 'updating' tree-ring chronologies using regional curve standardisation: Re-processing 1500 years of Torneträsk density and ring-width data. The Holocene, 23(3), pp.364–373. doi:10.1177/0959683612460791.

680

Moore, J.J., Hughen, K.A., Miller, G.H. and Overpeck, J.T. (2001). Journal of Paleolimnology, [online] 25(4), pp.503–517. doi:10.1023/a:1011181301514.

Mulcahy, J.P., Johnson, C., Jones, C.G., Povey, A.C., Scott, C.E., Sellar, A., Turnock, S.T., Woodhouse, M.T., Abraham,
685 N.L., Andrews, M.B., Bellouin, N., Browse, J., Carslaw, K.S., Dalvi, M., Folberth, G.A., Glover, M., Grosvenor, D.P., Hardacre, C., Hill, R. and Johnson, B. (2020). Description and evaluation of aerosol in UKESM1 and HadGEM3-GC3.1 CMIP6 historical simulations. Geoscientific Model Development, 13(12), pp.6383–6423. doi:10.5194/gmd-13-6383-2020.

Oppenheimer, C. (2003). Ice core and palaeoclimatic evidence for the timing and nature of the great mid-13th century
690 volcanic eruption. International Journal of Climatology, 23(4), pp.417–426. doi:10.1002/joc.891.

Palais, J.M., Germani, M.S. and Zielinski, G.A. (1992). Inter-hemispheric Transport of Volcanic Ash from a 1259 A.D. Volcanic Eruption to the Greenland and Antarctic Ice Sheets. Geophysical Research Letters, 19(8), pp.801–804. doi:10.1029/92gl00240.

695

Pinto, J.P., Turco, R.P. and Toon, O.B. (1989). Self-limiting physical and chemical effects in volcanic eruption clouds. Journal of Geophysical Research, [online] 94(D8), p.11165. doi:10.1029/jd094id08p11165.

Porter, T.J., Pisaric, M.F.J., Kokelj, S.V. and deMontigny, P. (2013). A ring-width-based reconstruction of June–July
700 minimum temperatures since AD 1245 from white spruce stands in the Mackenzie Delta region, northwestern Canada. Quaternary Research, 80(2), pp.167–179. doi:10.1016/j.yqres.2013.05.004.

Robock, A. (2000). Volcanic eruptions and climate. Reviews of Geophysics, [online] 38(2), pp.191–219. doi:10.1029/1998rg000054.

705

Robock, A. (2005). Cooling following large volcanic eruptions corrected for the effect of diffuse radiation on tree rings. Geophysical Research Letters, 32(6). doi:10.1029/2004gl022116.

Robock, A. (2020). Comment on 'No consistent ENSO response to volcanic forcing over the last millennium'. Science,
710 [online] 369(6509). doi:10.1126/science.abc0502.

Rydval, M., Loader, N.J., Gunnarson, B.E., Druckenbrod, D.L., Linderholm, H.W., Moreton, S.G., Wood, C.V. and Wilson, R. (2017). Reconstructing 800 years of summer temperatures in Scotland from tree rings. Climate Dynamics, 49(9-10), pp.2951–2974. doi:10.1007/s00382-016-3478-8.

715

Saliba, G. (2017). Cultural Implications of Natural Disasters: Historical Reports of the Volcano Eruption of July, 1256 CE. Transcultural Research – Heidelberg Studies on Asia and Europe in a Global Context, [online] pp.139–154. doi:10.1007/978-3-319-49163-9_7.

720 Schneider, L., Smerdon, J.E., Büntgen, U., Wilson, R.J.S., Myglan, V.S., Kirdyanov, A.V. and Esper, J. (2015). Revising midlatitude summer temperatures back to A.D. 600 based on a wood density network. Geophysical Research Letters, 42(11), pp.4556–4562. doi:10.1002/2015gl063956.

Sellar, A.A., Jones, C.G., Mulcahy, J.P., Tang, Y., Yool, A., Wiltshire, A., O'Connor, F.M., Stringer, M., Hill, R., Palmieri,
725 J., Woodward, S., Mora, L., Kuhlbrodt, T., Rumbold, S.T., Kelley, D.I., Ellis, R., Johnson, C.E., Walton, J., Abraham, N.L. and Andrews, M.B. (2019). UKESM1: Description and Evaluation of the U.K. Earth System Model. Journal of Advances in Modeling Earth Systems, 11(12), pp.4513–4558. doi:10.1029/2019ms001739.

730   Sigl, M., Winstrup, M., McConnell, J.R., Welten, K.C., Plunkett, G., Ludlow, F., Büntgen, U., Caffee, M., Chellman, N., Dahl-Jensen, D., Fischer, H., Kipfstuhl, S., Kostick, C., Maselli, O.J., Mekhaldi, F., Mulvaney, R., Muscheler, R., Pasteris, D.R., Pilcher, J.R. and Salzer, M. (2015). Timing and climate forcing of volcanic eruptions for the past 2,500 years. Nature, [online] 523(7562), pp.543–549. doi:10.1038/nature14565.

735   Stevenson, S., Fasullo, J.T., Otto-Bliesner, B.L., Tomas, R.A. and Gao, C. (2017). Role of eruption season in reconciling model and proxy responses to tropical volcanism. Proceedings of the National Academy of Sciences, 114(8), pp.1822–1826. doi:10.1073/pnas.1612505114.

Stevenson, S., Overpeck, J.T., Fasullo, J., Coats, S., Parsons, L., Otto-Bliesner, B., Ault, T., Loope, G. and Cole, J. (2018). Climate Variability, Volcanic Forcing, and Last Millennium Hydroclimate Extremes. Journal of Climate, [online] 31(11),
740   pp.4309–4327. doi:10.1175/jcli-d-17-0407.1.

Stoffel, M., Khodri, M., Corona, C., Guillet, S., Poulain, V., Bekki, S., Guiot, J., Luckman, B.H., Oppenheimer, C., Lebas, N., Beniston, M. and Masson-Delmotte, V. (2015). Estimates of volcanic-induced cooling in the Northern Hemisphere over the past 1,500 years. Nature Geoscience, 8(10), pp.784–788. doi:10.1038/ngeo2526.

745
Stothers, R.B. (2000). Climatic and Demographic Consequences of the Massive Volcanic Eruption of 1258. Climatic Change, 45(2), pp.361–374. doi:10.1023/a:1005523330643.

Stothers, Richard B. (2005). Stratospheric Transparency Derived from Total Lunar Eclipse Colors, 1801–1881. Publications
750   of the Astronomical Society of the Pacific, [online] 117(838), pp.1445–1450. doi:10.1086/497016.

Tejedor, E., Steiger, N.J., Smerdon, J.E., Serrano-Notivoli, R. and Vuille, M. (2021). Global hydroclimatic response to tropical volcanic eruptions over the last millennium. Proceedings of the National Academy of Sciences, 118(12), p.e2019145118. doi:10.1073/pnas.2019145118.

755
Timmreck, C., Lorenz, S.J., Crowley, T.J., Kinne, S., Raddatz, T.J., Thomas, M.A. and Jungclaus, J.H. (2009). Limited temperature response to the very large AD 1258 volcanic eruption. Geophysical Research Letters, 36(21). doi:10.1029/2009gl040083.

760   Toohey, M., Krüger, K., Niemeier, U. and Timmreck, C. (2011). The influence of eruption season on the global aerosol evolution and radiative impact of tropical volcanic eruptions. Atmospheric Chemistry and Physics, 11(23), pp.12351–12367. doi:10.5194/acp-11-12351-2011.

Toohey, M. and Sigl, M. (2017). Volcanic stratospheric sulfur injections and aerosol optical depth from 500 BCE to
765   1900 CE. Earth System Science Data, 9(2), pp.809–831. doi:10.5194/essd-9-809-2017.

Vidal, C.M., Komorowski, J.-C., Métrich, N., Pratomo, I., Kartadinata, N., Prambada, O., Michel, A., Carazzo, G., Lavigne, F., Rodysill, J., Fontijn, K. and Surono (2015). Dynamics of the major plinian eruption of Samalas in 1257 A.D. (Lombok, Indonesia). Bulletin of Volcanology, 77(9). doi:10.1007/s00445-015-0960-9.
770
Vidal, C.M., Métrich, N., Komorowski, J.-C., Pratomo, I., Michel, A., Kartadinata, N., Robert, V. and Lavigne, F. (2016). The 1257 Samalas eruption (Lombok, Indonesia): the single greatest stratospheric gas release of the Common Era. Scientific Reports, [online] 6(1). doi:10.1038/srep34868.

775   Vinther, B.M., Jones, P.D., Briffa, K.R., Clausen, H.B., Andersen, K.K., Dahl-Jensen, D. and Johnsen, S.J. (2010). Climatic signals in multiple highly resolved stable isotope records from Greenland. Quaternary Science Reviews, [online] 29(3-4), pp.522–538. doi:10.1016/j.quascirev.2009.11.002.

Wade, D.C., Vidal, C.M., Abraham, N.L., Dhomse, S., Griffiths, P.T., Keeble, J., Mann, G., Marshall, L., Schmidt, A. and
780 Archibald, A.T. (2020a). Reconciling the climate and ozone response to the 1257 CE Mount Samalas eruption. Proceedings of the National Academy of Sciences, 117(43), pp.26651–26659. doi:10.1073/pnas.1919807117.

Wade, D.C., Vidal, C.M., Abraham, N.L., Dhomse, S., Griffiths, P.T., Keeble, J., Mann, G., Marshall, L., Schmidt, A. and Archibald, A.T. (2020b). Reconciling the climate and ozone response to the 1257 CE Mount Samalas eruption. Proceedings
785 of the National Academy of Sciences, 117(43), pp.26651–26659. doi:10.1073/pnas.1919807117.

Wiles, G.C., D'Arrigo, R.D., Barclay, D., Wilson, R.S., Jarvis, S.K., Vargo, L. and Frank, D. (2014). Surface air temperature variability reconstructed with tree rings for the Gulf of Alaska over the past 1200 years. The Holocene, 24(2), pp.198–208. doi:10.1177/0959683613516815.
790
William Wayne Farris (2006). Japan's medieval population : famine, fertility, and warfare in a transformative age. Honolulu: University Of Hawai'i Press. ISBN-13: 9780824834241

Wilson, R., Anchukaitis, K., Briffa, K.R., Büntgen, U., Cook, E., D'Arrigo, R., Davi, N., Esper, J., Frank, D., Gunnarson, B.,
795 Hegerl, G., Helama, S., Klesse, S., Krusic, P.J., Linderholm, H.W., Myglan, V., Osborn, T.J., Rydval, M., Schneider, L. and Schurer, A. (2016). Last millennium northern hemisphere summer temperatures from tree rings: Part I: The long term context. Quaternary Science Reviews, [online] 134, pp.1–18. doi:10.1016/j.quascirev.2015.12.005.

Zhang, P., Linderholm, H.W., Gunnarson, B.E., Björklund, J. and Chen, D. (2016). 1200 years of warm-season temperature
800 variability in central Scandinavia inferred from tree-ring density. Climate of the Past, 12(6), pp.1297–1312. doi:10.5194/cp-12-1297-2016.

Zielinski, G.A., Mayewski, P.A., Meeker, L.D., Whitlow, S., Twickler, M.S., Morrison, M., Meese, D.A., Gow, A.J. and Alley, R.B. (1994). Record of Volcanism Since 7000 B.C. from the GISP2 Greenland Ice Core and Implications for the
805 Volcano-Climate System. Science, 264(5161), pp.948–952. doi:10.1126/science.264.5161.948.